



**HAL**  
open science

# Finite element analysis of the mechanical performance of self-expanding endovascular stents made with new nickel-free superelastic $\beta$ -titanium alloys

Tianyu Jia, Dominique Guines, Denis Laillé, Lionel Leotoing, Thierry Gloriant

## ► To cite this version:

Tianyu Jia, Dominique Guines, Denis Laillé, Lionel Leotoing, Thierry Gloriant. Finite element analysis of the mechanical performance of self-expanding endovascular stents made with new nickel-free superelastic  $\beta$ -titanium alloys. *Journal of the mechanical behavior of biomedical materials*, 2024, *Journal of the Mechanical Behavior of Biomedical Materials*, 151, pp.106345. 10.1016/j.jmbbm.2023.106345 . hal-04395165

**HAL Id: hal-04395165**

**<https://hal.science/hal-04395165>**

Submitted on 1 Feb 2024

**HAL** is a multi-disciplinary open access archive for the deposit and dissemination of scientific research documents, whether they are published or not. The documents may come from teaching and research institutions in France or abroad, or from public or private research centers.

L'archive ouverte pluridisciplinaire **HAL**, est destinée au dépôt et à la diffusion de documents scientifiques de niveau recherche, publiés ou non, émanant des établissements d'enseignement et de recherche français ou étrangers, des laboratoires publics ou privés.

# Finite element analysis of the mechanical performance of self-expanding endovascular stents made with new nickel-free superelastic $\beta$ -titanium alloys

Tianyu Jia<sup>1</sup>, Dominique Guines<sup>2</sup>, Denis Laillé<sup>1</sup>, Lionel Leotoing<sup>2</sup>, Thierry Gloriant<sup>1,\*</sup>

<sup>1</sup> *University of Rennes, INSA Rennes, CNRS UMR 6226 ISCR, 35000 Rennes, France*

<sup>2</sup> *University of Rennes, INSA Rennes, LGCGM, EA 3913, 35000 Rennes, France*

\*[Thierry.Gloriant@insa-rennes.fr](mailto:Thierry.Gloriant@insa-rennes.fr) (T. Gloriant)

## Abstract

New Ni-free superelastic  $\beta$ -titanium alloys from the Ti-Zr-Nb-Sn system have been designed in this study to replace the NiTi alloy currently used for self-expanding endovascular stents. The simulation results, carried out by finite element analysis (FEA) on two  $\beta$ -type Ti-Zr-Nb-Sn alloys using a commonly used superelastic constitutive model, were in good agreement with the experimental uniaxial tension data. An ad-hoc self-expanding coronary stent was specifically designed for the present study. To assess the mechanical performance of the endovascular stents, a FEA framework of the stent deployed in the arterial system was established, and a simply cyclic bending loading was proposed. Six comparative simulations of three superelastic materials (including NiTi for comparison) and two arterial configurations were successfully conducted. The mechanical behaviours of the stents were analysed through stress localization, the increase in artery diameter, contact results, and distributions of mean and alternating strain. The simulation results show that the Ti-22Zr-11Nb-2Sn (at. %) alloy composition for the stent produces the largest contact area (9.92 mm<sup>2</sup>) and radial contact force (49.5 mN) on the inner surface of the plaque and a higher increase in the stenotic artery diameter (70 %) after three vascular bending cycles. Furthermore, the Ti-22Zr-11Nb-2Sn stent exhibited sufficient crimping capacity and reliable mechanical performance during deployment and cyclic bending, which could make it a suitable choice for self-expanding coronary stents. In this work, the implementation of finite element analysis has thus made it possible to propose a solid basis for the mechanical evaluation of these stents fabricated in new Ni-free superelastic  $\beta$ -Ti alloys.

**Keywords:** titanium alloys, superelastic property, self-expanding stents, finite element analysis

## 1. Introduction

Metallic endovascular stents are expandable coil-like scaffold structures, which are currently used in most angioplasty procedures to prevent arteries from clogging. NiTi material is widely used in biomedical fields for such application due to its shape memory and pseudo-elastic (or superelastic) properties as peripheral or cardiovascular stents (Duerig et al., 1999; Stoeckel et al., 2004), bone staples (Krone et al., 2005) and self-expanding inferior vena cava filters (Grassi, 1991). At selected temperatures, NiTi performs a superelastic effect, enabling large recoverable deformation strain (more than 8.0%) through the reversible martensitic phase transformation from the cubic B2 phase (austenite) to the monoclinic B19' phase (martensite), combined with the twinning/detwinning of martensite (Otsuka and Ren, 2005). However, studies on the biocompatibility of NiTi revealed that such material may induce severe allergic reactions, hypersensitivity and cytotoxicity due to its nickel content, whereas these phenomena were not observed in Ni-free titanium alloys (Gotman, 1997; Steinemann, 1996; Wever et al., 1997). Thus, the focus of research on superelastic biomaterials has moved towards the development of nickel-free superelastic titanium alloys (Ramezannejad et al., 2019). As a result, Ni-free  $\beta$ -Ti alloys based on biocompatible alloying elements such as Ta, Zr, Mo and Nb (Steinemann, 1998) have been developed as alternative superelastic biomedical materials (Miyazaki et al., 2006). Indeed, for certain compositions, these  $\beta$ -Ti alloys can also present a stress-induced martensitic transformation (SIM) from the parent cubic  $\beta$  phase to the orthorhombic martensitic  $\alpha''$  phase. However, the first generation of alloys developed from the Ti-Nb-based system showed lower recovery strains (less than 3.0 %) compared to NiTi alloys. Therefore, other superelastic  $\beta$ -Ti alloys from the Ti-Zr-based system have recently been designed to obtain higher recovery properties (Gao et al., 2020; Pavón et al., 2015), and our group has elaborated by cold-crucible levitation melting on new compositions such as Ti-20Zr-3Mo-3Sn (at. %), Ti-24Zr-10Nb-2Sn (at.%) (Ti24102) and Ti-22Zr-11Nb-2Sn (at.%) (Ti22112) (Cabon, 2021) which show by tensile tests recoverable strains reaching 3.5%, 3.6% and 4.7%, respectively. The new elaborated Ti22112 and Ti24102 alloys mentioned above both present a single  $\beta$  phase microstructure and display high superelasticity after flash treatment at 700 °C for 5 min due to the stress-induced martensitic transformation that occurs. In these alloys, niobium acts as  $\beta$ -stabilizing element and tin has been used to suppress the formation of  $\omega$  phase (Ijaz et al., 2014). The suppression of athermal  $\omega$  phase contributes to a higher recovery strain and its combination with zirconium also improves superelasticity (Gao et al., 2019).

This article, therefore, aims to evaluate the mechanical performance of these new biocompatible alloys for the fabrication of self-expanding stents and to compare them to the commercial NiTi alloy currently used for this application. For this purpose, a self-expanding stent resembling the commercial models was designed in this study and simulated with the three chosen superelastic materials (NiTi, Ti22112 and Ti24102) to evaluate the potential of the new nickel-free superelastic titanium alloys. Simulations by finite element analysis (FEA) of stents deployment and cyclic bending were implemented in a stenotic artery compared with a straight artery. Multiple numerical variables including stents stress distribution, artery diameter change and total contact results, were analysed to highlight differences between materials.

## **2. Geometry and materials**

### *2.1. Self-expanding stent model*

A 3D model of the superelastic coronary stent was chosen to resemble a typical design of Endeavor™ stent in the commercial FEA software Abaqus/Explicit 2021 which is a cylindrical slotted tube manufactured as a fully expanded shape. Even though self-expanding stents are more widely used for peripheral arteries, they can also be used for coronary arteries according to the literature. For instance, Amoroso et al. firstly confirmed the clinical feasibility and safety of a self-expanding stent in the coronary artery (Amoroso et al., 2011). Favourable outcomes in the left main coronary artery were also reported (Lu et al., 2018). The geometry model of the stent is illustrated in Fig. 1. The stent is composed of eight rings (Fig. 1 (a)) along the axial direction and each ring is composed of six circumferential patterns (Fig. 1 (b)) connecting peak-to-peak (Fig. 1 (c)). The fully released stent has an outer diameter ( $D_s$ ) of 5.12 mm, a length of 24.2 mm, and a thickness of 0.24 mm.

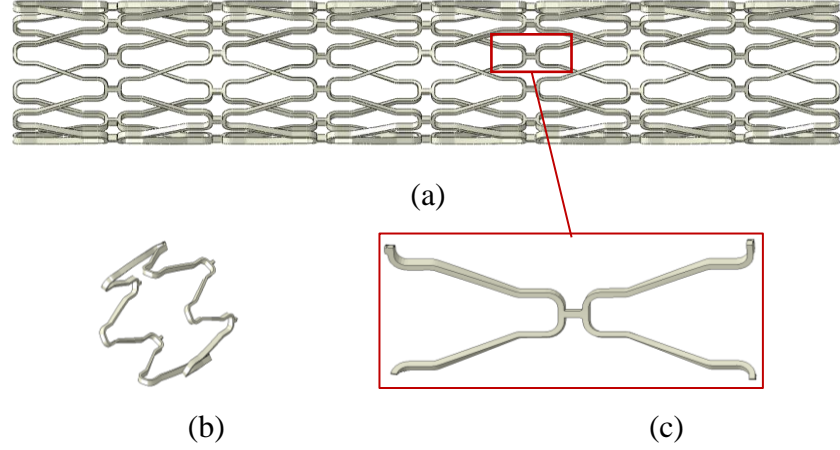


Fig. 1. The self-expanding stent consists of (a) eight rings in the longitudinal direction; (b) each ring consists of six circumferential patterns; (c) the close cell stent is linked peak-to-peak in the red box.

As mentioned, the superelastic  $\beta$ -Ti alloy undergoes a reversible phase transformation from the cubic  $\beta$  phase to the orthorhombic  $\alpha'$  martensitic phase under stress. The stress-strain pseudo-elastic behaviour and its characteristic parameters are described with using the built-in SUPERELASTIC material model in ABAQUS (Fig. 2).

The parameters of the pseudo-elastic material model were calibrated from uniaxial tension experiments after fitting FEA curves in Table 1. The value of the tension-compression asymmetry observed in NiTi was set equal to 0.74 (Liu et al., 1998; Org as and Favier, 1998) and also assumed to be 0.74 for  $\beta$ -Ti alloys, which was necessary to fix because compression data in such alloys are not known from experiments. Thus, the implemented phenomenological model was compared to experimental data under uniaxial tension and the results are presented in Fig. 3.

Table 1. Parameters of the superelastic stent materials: NiTi (Meoli et al., 2013), Ti24102 and Ti22112 (Cabon, 2021)

Parameters	Description	NiTi	Ti24102	Ti22112
$E_A$	Austenite Young's modulus (MPa)	51100	65000	55000
$E_M$	Martensite Young's modulus (MPa)	51100	36000	45000
$\nu_A$	Austenite Poisson's ratio	0.3	0.33	0.33
$\nu_M$	Martensite Poisson's ratio	0.3	0.33	0.33
$\varepsilon_L$	Transformation strain	0.0492	0.036	0.047
$\sigma_{tL}^S$	Start of transformation (loading) (MPa)	416	350	415
$\sigma_{tL}^E$	End of transformation (loading) (MPa)	442	485	570



## 2.2. Artery and plaque

A model of the diseased artery consisting of a single-layer straight vessel wall and an atherosclerotic plaque was built as shown in Fig. 4. The straight vessel wall has an inner diameter ( $D_a$ ) of 4 mm with a stent-to-vessel oversizing ratio of 1.25. Few statistical data on plaque shape are currently available. Generally, the plaque is estimated to be uniform in the circumferential direction, and its thickness ( $t$ ) is modeled according to the modified Hicks-Henne function (Pant et al., 2012):

$$t = t_b + \left( \frac{D_a}{2} R_s - t_b \right) \sin \left( \frac{x}{L_p} \pi \right)^s, \quad 0 < x < L_p, \quad (1)$$

where  $t_b$  is the base thickness of the plaque,  $L_p$  is the plaque length,  $R_s$  is the stenosis rate and  $s$  is the sharpness of the plaque. The simplified stenotic vessel model with high sharpness is shown in Fig. 4. The length of the whole artery is 40 mm, and the values of  $t_b$ ,  $L_p$ ,  $R_s$  and  $s$  are respectively 0.5 mm, 30 mm, 45% and 10.  $A$  represents the height of the bump (analogous to the peak stenosis), which is equal to  $\frac{D_a}{2} * R_s$ . To fully investigate the supporting capability of the stent, a comparative simulation of a healthy vessel without plaque was also carried out.

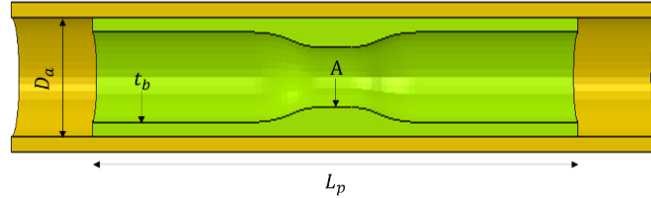


Fig. 4. A simplified stenotic vessel with high-sharpness plaque. The yellow section represents the artery and the green shape represents the plaque

The non-linear material properties of both the artery and plaque are described using the Hyperelastic isotropic constitutive model as the third-order reduced polynomial strain energy density function:

$$U = \sum_{i=1}^3 C_i (I_1 - 3)^i, \quad (2)$$

where  $C_i$  are material coefficients, and  $I_1$  is the first strain invariant of the Cauchy-Green deformation tensor.

To model the inelasticity and damage of atherosclerotic plaque, a perfect plasticity model is employed in this study (Dordoni et al., 2014). The actual rupture stress is considered as yield stress, as noted in a previous research paper (Gastaldi et al., 2010). The material coefficients

of the diseased coronary plaque tissue are listed in Table 2, with a yield point of 0.158 MPa defined on the basis on a recent study (Lei et al., 2019). The nominal stress-strain curves for both the artery and the plaque can be visualized in Fig. 5.

Table 2. Coefficients of the artery and plaque (Lei et al., 2019).

Material	$C_1$ (MPa)	$C_2$ (MPa)	$C_3$ (MPa)
Artery	1.05E-2	1.94E-2	1.1E-2
Plaque	4.62E-2	-1.47E-2	4.95E-3

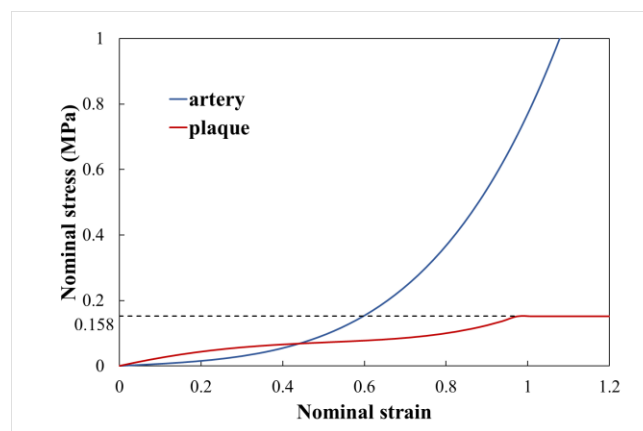


Fig. 5. Constitutive behaviour of the artery and plaque. Values of the artery and the plaque are in blue and red lines, respectively.

### 3. Modelling

#### 3.1. Mesh

Three separate parts were considered: the stenotic artery (including artery and plaque), the stent, and the sheath used for crimping the stent. The stent was meshed using eight-node linear elements with reduced integration and hourglass control (C3D8R) as presented in Fig. 6 (a). The total number of elements to mesh the stent was 55,632 based on mesh sensitivity studies. On the other hand, the sheath was modelled as a shell and discretized with reduced 4-node doubly curved shell elements that enhanced hourglass control and finite membrane strains (S4R). Both the healthy and stenotic artery models were meshed with hybrid incompatible 8-node linear brick elements (C3D8HI), as shown in Fig. 6 (b).

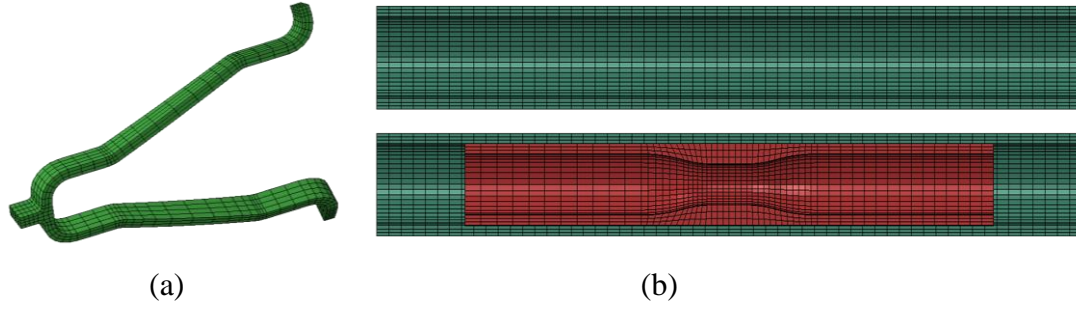


Fig. 6. Mesh of (a) stent, (b) straight and stenotic artery.

To ensure appropriate mesh refinement, a sensitivity analysis was conducted using a single stent ring model and the corresponding section of the artery-plaque system. The maximum radial displacement of the vessel ( $U_r$ ) following device deployment as well as the maximum and minimum principal strain ( $\varepsilon^1$ ,  $\varepsilon^3$ ) in the stent, were evaluated as part of this analysis. The vessel-to-stent element number ratio was varied while holding the number of stent elements constant, and three ratios (0.15, 0.5, and 1) were examined. The results showed that the finest mesh of the vessel provided the most accurate displacement field, although the difference in maximum values between ratios of 0.5 and 1 was not significant as shown in Fig. 7. Therefore, a vessel-to-stent element number ratio of 0.5 was determined to provide the best balance between result accuracy and computational time.

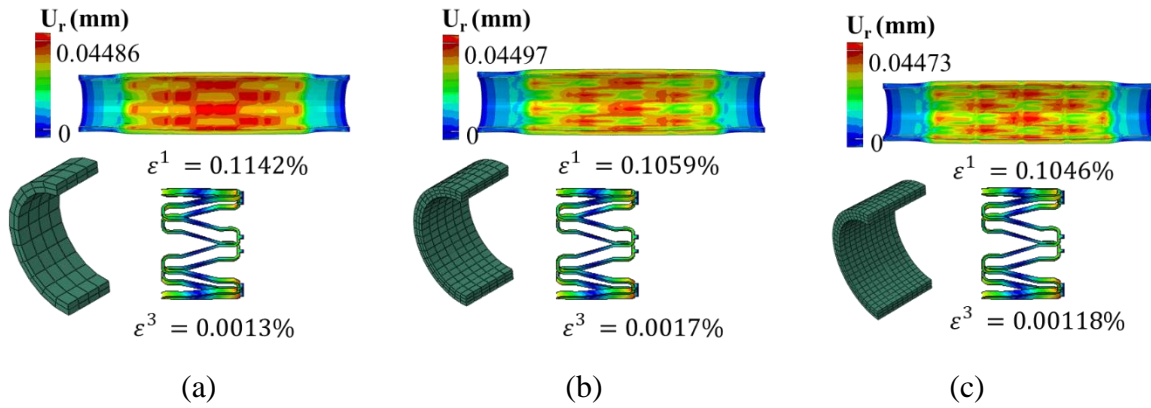


Fig. 7. Mesh sensitivity study on the system at the end of contact equilibrium. The ratio between the element number of artery and stent was 0.15 (a), 0.5 (b) and 1(c).

### 3.2. Boundary conditions and interaction

The stenting procedure simulation was carried out using ABAQUS 2021/Explicit due to the high level of nonlinearity present, including material, geometric and complex interactions. The entire process was divided into five distinct analysis steps: stent crimping, stent pre-

stretching, free expansion of the stent, contact stabilization, and cyclic bending. These steps are described in detail below:

- Initial configuration: The initial assembly of the stent, sheath, and artery was set up in a coaxial arrangement. The sheath's inner diameter was slightly larger than the outer diameter of the stents (Fig. 8 (a)).
- Crimping of the stent into a sheath: To reproduce the stress/strain field in the stent crimping. The surface-to-surface contact pair between the outer surface of the stent and the inner surface of the sheath was created with a tangent penalty friction coefficient of 0.2 (Dordoni et al., 2014; Nikanorov et al., 2008; Vad et al., 2010). A negative radial displacement was imposed on the sheath to crimp the stent until its diameter was 1 mm smaller than the plaque's inner diameter (Fig. 8 (b)). This resulted in a considerable amount of strain energy stored in the stent for subsequent self-expansion. The self-contact interaction with the outer surface of the stent is activated from this step to avoid the self-penetration.
- Pre-stretching of the stent: To avoid sudden energy change in the system, the diameter of the sheath was increased until it was in contact with the inner surface of the artery. This was achieved by imposing a positive radial displacement on the sheath, as shown in Fig. 8 (c). This additional step helped to prevent convergence difficulties in the Static General analysis step.
- Self-expansion of the stent: The sheath was removed so the stent was allowed to self-expand. The sheath was subjected to translation displacement until it was away from the vessel (Fig. 8 (d)). The interaction between the sheath and the stent was deactivated, and the sheath no longer worked in the system. A surface-to-surface contact was created between the inner surface of the artery and the outer surface of the stent with a penalty friction coefficient of 0.2 (Dordoni et al., 2014).
- Equilibrium of the whole system: A separate step was included to reach equilibrium between the stent and the stenotic vessel (Fig. 8 (e)), which helped to avoid convergence difficulties. For simplification, the steps (Fig. 8 (c)-(e)) are named as deployment.
- Cyclic bending: To analyse the stent's mechanical behaviour, cyclic vascular bending was performed to change the artery-plaque system's curvature (Fig. 8 (f)).

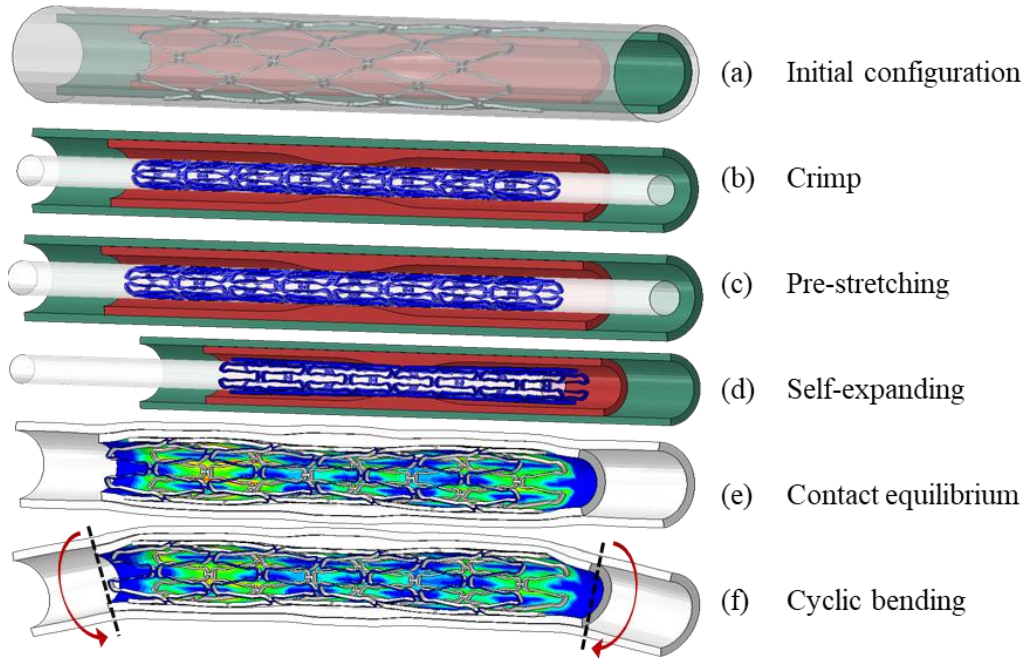


Fig. 8. Five typical simulation states during the stenting procedure.

A vascular bending angle of  $12^\circ$  was applied to induce a stent curvature of  $0.0106 \text{ rad.mm}^{-1}$  (Xu et al., 2016). The contact ratio was defined as the actual contact area between stent and plaque divided by the value after deployment. The evolution of the contact area ratio with the number of cycles in the stenotic artery model implanted by the Ti2212 stent is illustrated in Fig. 9. At the end of a bending stage, the cross section of the vessel would change into an irregular elliptical shape leading to the change in the total contact area. However, it can be observed that the contact area reached stabilization after the first three cycles. Thus, the simulation performed only three loading-unloading cycles to balance computing time and result accuracy.

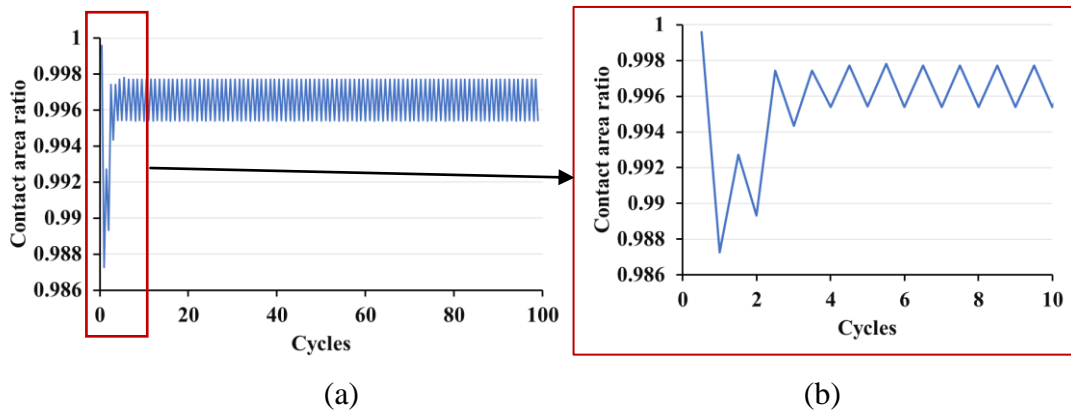


Fig. 9. The evolution of contact area ratio between the Ti2212 stent and the stenotic artery during (a) 100 bending cycles and red box identical to (b) the first ten cycles.

## 4. Results

### 4.1. Simulation results of stent deployment

Three simulations were conducted including straight vessels and stents made of NiTi (Model-1), Ti24102 (Model-2) and Ti22112 (Model-3) as well as three stents made of NiTi (Model-4), Ti24102 (Model-5) and Ti22112 (Model-6) implanted in the vessel with plaque.

After crimping, the maximum von Mises stress in the stents of stenotic cases were approximately 1.8 times the values for the non-stenotic models as it is shown in Table 3 because of the difference in the radial displacement applied to the stents. None of the stents experienced plastic deformation during crimping. After deployment, the maximum von Mises stress in all the stents was reduced by more than 50 % compared with those after crimping.

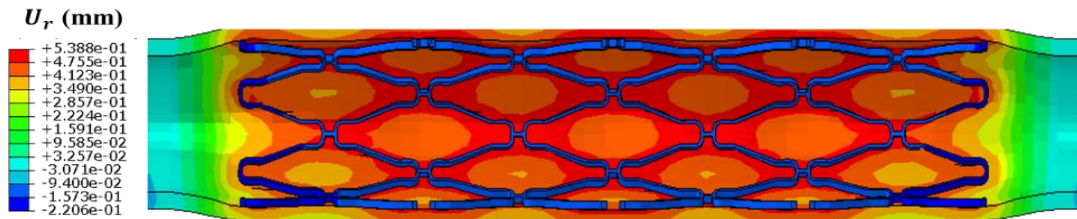
The contour plots of radial displacement ( $U_r$ ) for the Ti22112 models after deployment are displayed in Fig. 10 (a) and (b). Fig. 10 (c) presents the results of Model-6 at the end of the third loading stage. All stents fit well in the stenotic artery during bending loading. The artery diameter of the stented region was larger than that of the non-stented region because the stents expanded outward onto the vessel. All stents in the straight vessels expanded uniformly in the longitudinal direction. The magnitude of total force due to contact pressure between the stents and vessels (termed as CFNM in Abaqus) provided the tensile force on the arteries. The NiTi stent produced the smallest contact area of  $4.05 \text{ mm}^2$  and a total contact force of 0.01 mN on the artery surface. The contact area and the total contact force were  $4.07 \text{ mm}^2$  and 0.014 mN on the artery surface with the Ti22112 stent. The Ti24102 stent produced a total contact force of 0.013 mN, close to Ti22112, but the largest contact area ( $4.17 \text{ mm}^2$ ). These small differences in the total contact area and force of three stents in the straight vessels are due to the low oversizing rate of the straight vessel and the comparable strength of Ti22112 and Ti24102.

The presence of plaque significantly influenced the stents deformation as shown in Fig. 10. The implantation of the stents did not eliminate stenosis of the diseased vessel. The stenotic artery still has the minimum lumen at the stenosis peak corresponding to a slight tissue prolapse. The Fig. 11 compares the maximum increase in the artery inner diameter of all stents. The Ti22112 stent produced the most significant increment in the stenotic vessel diameter and the largest contact area than NiTi and Ti24102 stents with a residual stenosis rate of 10.7 %. Additionally, the total radial contact force was found to correlate with the increment in the vessel diameter after stent deployment. Total radial contact forces acting on the stenotic vessel surface were found to be 2.52, 2.06 and 2.60 mN for the NiTi, Ti24102

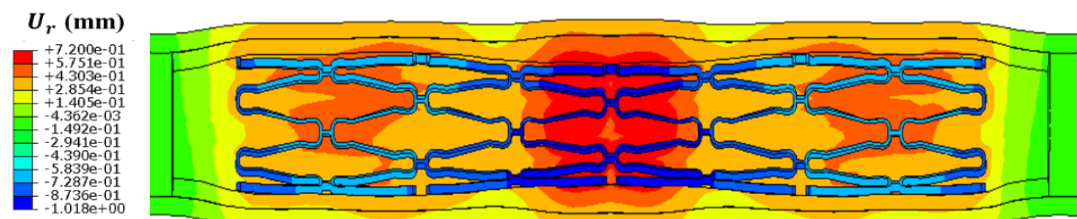
and Ti22112 stents, respectively. The Ti22112 stent exhibited the highest outward force against the plaque. A higher expansion force of self-expanding stents after implantation is thought to help overcome external compression and further restenosis according to the regulatory guideline ASTM F3067-14.

Table 3. Simulation results for all stents after deployment.

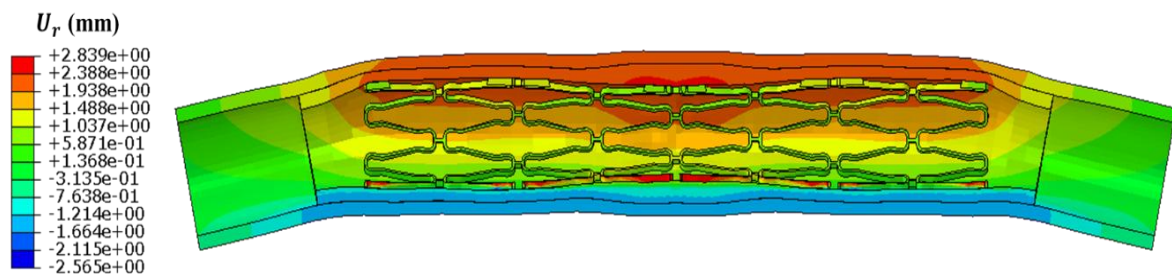
Indicators	No plaque			With plaque		
	Model-1	Model-2	Model-3	Model-4	Model-5	Model-6
Stent material	NiTi	Ti24102	Ti22112	NiTi	Ti24102	Ti22112
<i>After crimping</i>						
Max. Mises stress (MPa)	375.2	399.1	402.8	686.4	710	684.2
<i>After deployment</i>						
Max. Mises stress (MPa)	106.6	117.2	110.1	420.4	295.2	448.7
Total contact area (mm <sup>2</sup> )	4.05	4.17	4.07	9.31	8.86	9.96
Total force due to contact pressure (mN)	0.010	0.013	0.014	2.52	2.06	2.60



(a) Model-3: without plaque



(b) Model-6: with plaque



(c) Model-6: during bending

Fig. 10. Radial displacement contour plots of the models (a) (b) after Ti22112 stent deployment and (c) at the end of loading stage in the third cycle.

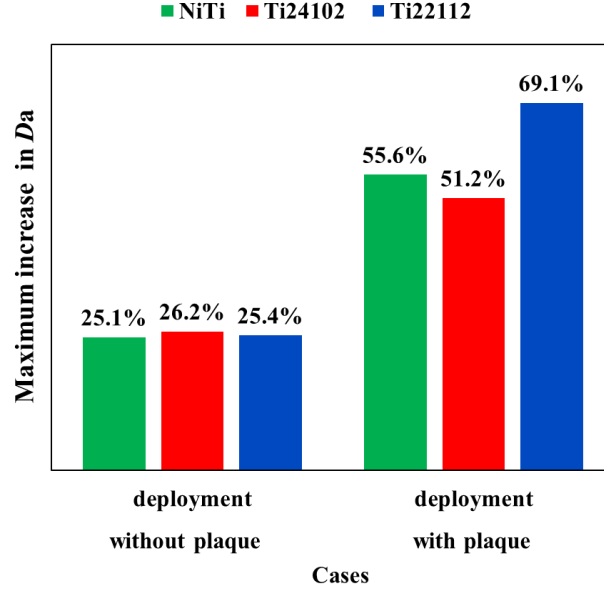


Fig. 11. Maximum increases in diameter of straight and stenotic arteries  $D_a$  (%) after being implanted with Ti24102, Ti22112 and NiTi stents.

#### 4.2. Simulation results of cyclic bending

To understand the stress state of the deployed stent during vascular bending, a diagram of the triaxiality versus the Lode parameter for the Ti22112 stent implanted in the stenotic artery (Model-6) was plotted in Fig. 12 at the end of the last bending loading step. Similar stress states were observed in other models but are not presented. The stress triaxiality  $\eta_H$  is defined as the ratio of the hydrostatic stress  $\sigma_H$  to the von Mises equivalent or effective deviatoric stress  $\bar{\sigma}_{eq}$ . The Lode parameter  $L_P$  is a function of the third invariant of the stress deviator.  $\sigma^1$ ,  $\sigma^2$ , and  $\sigma^3$  are principal stresses. The quantities were defined by principal stresses in the following equations.

$$\eta_H = \frac{\sigma_H}{\bar{\sigma}_{eq}} = \frac{1}{3} \frac{\sigma^1 + \sigma^2 + \sigma^3}{\sqrt{\frac{1}{2}[(\sigma^1 - \sigma^2)^2 + (\sigma^2 - \sigma^3)^2 + (\sigma^3 - \sigma^1)^2]}}, \quad (3)$$

$$L_P = \frac{2\sigma^2 - \sigma^1 - \sigma^3}{\sigma^1 - \sigma^3}, \quad \#(4)$$

Both quantities,  $\eta_H$  and  $L_P$ , are independent of the stress intensity but dependent on the type of stress state. The sign of  $\eta_H$  helps characterize the dominant type of stress in a given stress state: a positive stress triaxiality is associated with a tension-dominated stress state, while all

the stress states relating to  $\eta_H < 0$  the material can be considered as predominately compressive. The Lode parameter can be combined with  $\eta_H$  to describe the stress state, ranging from axisymmetric tension ( $L_p = 1$ ) to biaxial tension with axisymmetric compression ( $L_p = -1$ ) and passing through in-plane shear. As illustrated by Fig. 12, the stent was obviously in a multi-axial stress state compared with the marks of those characteristic states. Generally, 52% of the elements were under the compression-dominated state ( $\eta_H < 0$ ) and 48% of the elements were under tension-dominated stress state ( $\eta_H > 0$ ). The elements of the stent predominantly experienced bidirectional tension (47% of all the elements) and bidirectional compression (50%), with a minor portion subject to triaxial compression (2%). Triaxial tension was observed in 1% of all the elements.

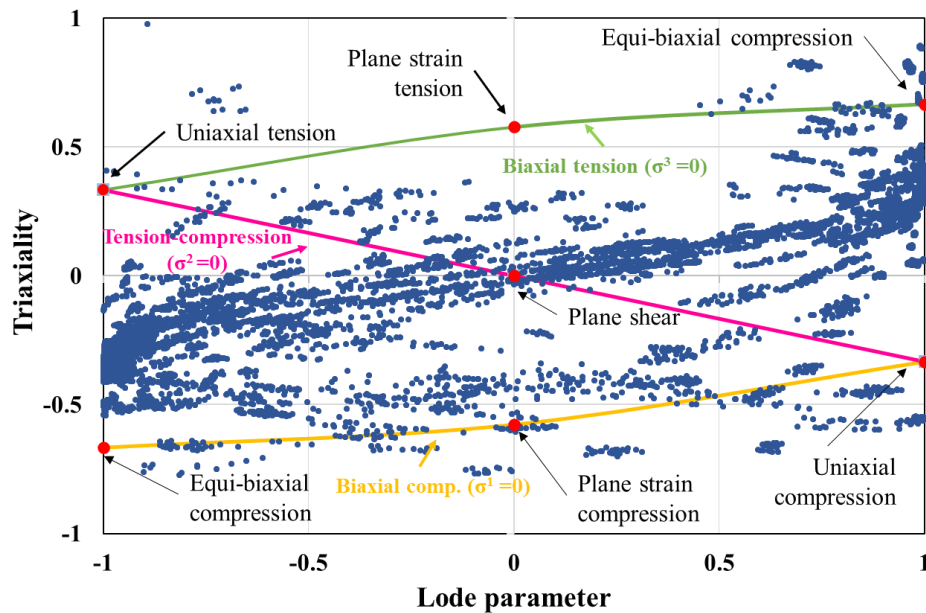


Fig. 12. Stress states in the space of the stress triaxiality and the Lode parameter of the whole stent at the end of the last bending loading step in the Model-6. Red marks highlight the characteristic states. The yellow, magenta and green curves show the relationship for biaxial compression ( $\sigma^1 = 0; \sigma^2, \sigma^3 < 0$ ), biaxial tension-compression ( $\sigma^1 > 0; \sigma^2 = 0, \sigma^3 < 0$ ), and biaxial tension ( $\sigma^1, \sigma^2 > 0; \sigma^3 = 0$ ), respectively.

The simulation results for all stents after cyclic bending was summarized in Table 4. Considering vascular bending, the Ti24102 stent has the largest contact area and produces the greatest increase in diameter of a straight vessel, followed by the Ti22112 and NiTi stents, as shown in Fig. 13. This trend is identical to the result obtained after deployment. However, the Ti22112 stent still produces a greater contact area and contact force on the stenotic artery

than NiTi and Ti24102 stents. After cyclic bending, the magnitudes of total forces due to contact pressure (termed as CFNM in Abaqus) on the stenotic vessel are 45.52, 45.29, and 49.50 mN with NiTi, Ti24102 and Ti22112 stents, respectively. The Ti22112 stent further improves the lumen gain but does not completely eliminate the stenosis, which exhibits an identical trend to the corresponding results obtained after deployment. For the same oversize, Ti22112 stent achieved the greatest reduction in stenosis followed by NiTi and Ti24102. The frictional force between stents and tissue is more pronounced in the longitudinal direction than in the radial and circumferential directions. As a result, only the total forces arising from longitudinal frictional stress, labelled as CFS3 in Abaqus, have been presented.

Table 4. Simulation results for all stents after cyclic bending.

Indicators	No plaque			With plaque		
	Model-1	Model-2	Model-3	Model-4	Model-5	Model-6
Stent material	NiTi	Ti24102	Ti22112	NiTi	Ti24102	Ti22112
Max. Mises stress (MPa)	105.6	116.4	109.1	430.3	294.6	391.2
Total contact area (mm <sup>2</sup> )	4.15	4.25	4.13	9.30	8.98	9.92
Total force due to contact pressure (mN)	2.2	0.18	1.6	45.52	45.29	49.50
Total force due to longitudinal frictional stress (mN)	0.09	0.10	0.11	0.53	0.86	0.39
Max. mean strain (%)	0.203	0.18	0.20	3.11	3.00	3.37
Max. alternating strain (%)	0.035	0.0325	0.0356	0.097	0.064	0.0546
Martensite volume fraction	0	0	0	2.89%	1.46%	5.36%

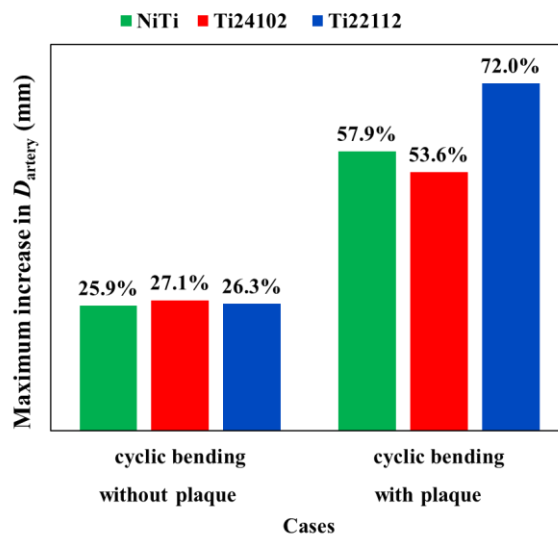


Fig. 13. Maximum increases in diameter of straight and stenotic arteries  $D_a$  (%) after three bending cycles.

The mean and alternate strains ( $\varepsilon_m$  and  $\varepsilon_a$ ) in each element of the stents were calculated for a loading cycle by the following equations:

$$\varepsilon_m = \frac{\varepsilon_{ij}^L + \varepsilon_{ij}^U}{2}, \quad (5)$$

$$\varepsilon_a = \left| \frac{\varepsilon_{ij}^L - \varepsilon_{ij}^U}{2} \right|, \quad (6)$$

which were derived from the strain tensors of the last sub-step of a loading ( $\varepsilon_{ij}^L$ ) and unloading ( $\varepsilon_{ij}^U$ ) step, and  $i, j=1, 2, 3$ . The first principal components of the mean and alternate strain were obtained by the postprocessor.

The first principal mean strain ( $\varepsilon_m^1$ ) contour plots of the Model-6 are plotted in Fig. 14. All the stents have the similar distribution of the mean strain for both arteries. The mean strain is distributed relatively evenly in the rings of the whole stent along the axial direction. The concentration of mean strain in each graft mainly occurs in curvature region.

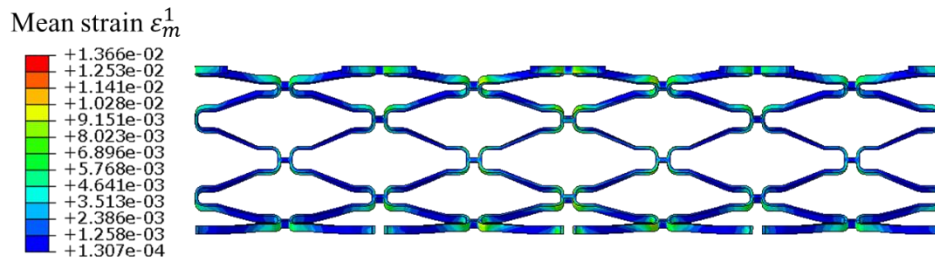
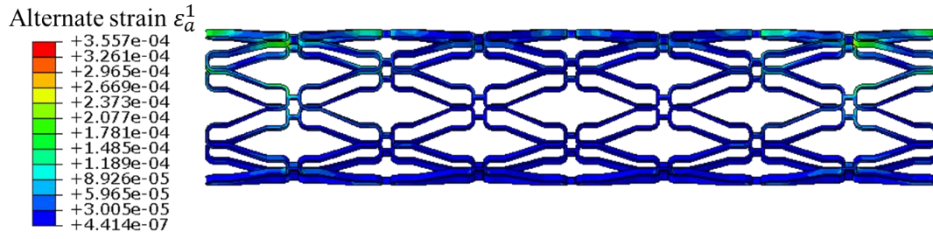
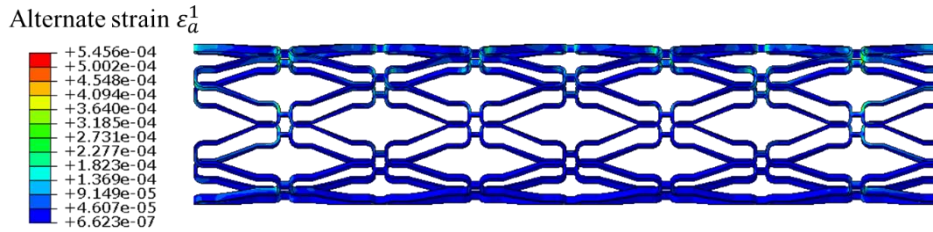


Fig. 14. First principal mean strain ( $\varepsilon_m^1$ ) contour plots of the Model-6 (Ti22112) in the stenotic artery. All the stents have the similar distribution of the mean strain for both arteries.

Under the cyclic boundary conditions, the first principal alternating strain ( $\varepsilon_a^1$ ) contour plots of the Ti22112 stents are shown in Fig. 15. The alternating strain is apparently concentrated in the curvature region of each stent graft especially at the two ends of the whole stent. For the stenotic artery case (Fig. 15 (b)), the alternating strain distribution is also concentrated in the curvature part, and the maximum value is situated at the upper peak of the plaque.



(a) Model-3



(b) Model-6

Fig. 15. First principal alternating strain  $\varepsilon_a^1$  contour plots of the Ti22112 stents in the artery without (a) and with (b) plaque.

## 5. Discussion

The non-uniform cylindrical morphology of stenosis can impact the interaction between the stent and the vessel. To address this issue, a simplified straight artery model with an arteriosclerosis stenosis of high sharpness was developed in this study to replicate their interaction with stents, rather than using patient-specific vessel models. Moreover, the shape of stenosis can vary greatly depending on factors such as sharpness, plaque peak point and stenosis rate. The distance of the plaque peak point was set to be 0.5 mm away from the baseline and the crimper diameter was consequently reduced to less than 2 mm.

Experimental methods for mechanical evaluation in such small-scale stents are difficult to design and implement during complex multi-step loading and FEA has been widely used to investigate the performance of NiTi stents in the coronary and carotid arteries (Auricchio et al., 2011; Wu et al., 2007). On the other hand, optimizing stents design to improve the performance of NiTi stents has been recently conducted using computational simulation (Chen et al., 2019; Mazurkiewicz et al., 2021; Russ et al., 2021). To date, much experimental research has been conducted on the performance of  $\beta$ -Ti alloys, in particular their mechanical and fatigue properties and their biocompatibilities. However, no research has focused on the numerical analysis of their functionalities for self-expanding stent devices. The present work aims to fill this gap by providing an effective simulating approach for evaluating the mechanical performance of  $\beta$ -Ti cardiovascular stents. To our knowledge, this work is the

first to evaluate new superelastic  $\beta$ -Ti self-expanding stents compared to common superelastic NiTi stents from the practical viewpoint.

When choosing the stent alloy, the capability to compress and expand are essential for the crimping-deployment and subsequent support for long service life. Our simulation first realized a good match with the experimental testing results of superelastic  $\beta$ -Ti alloys, using a currently available constitutive model built in Abaqus. With a verified constitutive model, a multi-step stenting procedure was established by FEA. The simulation demonstrated sufficient crimping capacity of new superelastic  $\beta$ -Ti stents and adaptability in the stenotic arteries during vascular bending. The curvature regions of the stents were subjected to large deformation but without plastic strain. FEA results showed that the maximum stress in all stents was not beyond the yield strength of materials, indicating no plastic deformation. These results are rather positive because it is known that the accumulation of permanent plastic strain can significantly affect the mechanical properties of superelastic alloys (Šittner et al., 2018) and cause functional degradation during cyclic loading (LePage et al., 2021). Furthermore, the stresses in stents were mainly concentrated in the curved region of stent grafts where the inner side of the stents underwent compression and the outer side experienced tension. Combined a  $\eta_H - L_p$  plot with the specific marked points, it is convenient to analyse the material behaviour of a stent implanted in the stenotic artery and subjected to various potential loading conditions. The detailed  $\eta_H - L_p$  plot (Fig. 12) in the Model-6 showed the multi-axial stress state of the stents. Overall, more elements underwent compression than tension, potentially minimizing the risk of plastic failure. Clearly identifying these distinct stress states in the stents will contribute to future failure design and the selection of appropriate criteria. It is essential to note that the tension-compression asymmetry assumed for superelastic alloys in this study is 0.74. Hence, considering the tension-compression asymmetry of those alloys is necessary to achieve more accurate results close to reality.

Based on the experimental results regarding the material behaviour of the alloys, it is interesting to note that Ti24102 stent exhibits a lower increase in the stenotic artery diameter compared to the NiTi stent (Fig. 11 and Fig. 13) although its intrinsic elastic modulus measured at the origin, i.e. its stiffness, is higher. In fact, during stent implantation, the stent is in a two-phase state containing austenite and martensite due to the deformation. In such case, it is the apparent modulus which must be considered and not the intrinsic modulus. As the modulus of the martensitic phase is lower in the case of the Ti24102 stent (Table 1), it can

be assumed that the apparent modulus is lower thus explaining why the Ti24102 stent exhibits the lowest contact force and increase in the stenotic artery diameter.

Additionally, the Ti22112 stents also has the largest total radial contact force during deployment and vascular bending, which helps reduce stent migration during the complex vessel movements. Moreover, the increase in the arterial system diameter was found to be correlated with the increase in the total radial contact force. Besides, the removal of the catheter and vascular bending induced frictional stress on the stents, and ~~too~~ excessively high axial friction will make stents out of place in extreme cases. In this work, all stents produced relatively low magnitudes of the total longitudinal frictional force and displacement. Compared to NiTi stents, Ti22112 stents introduced a lower longitudinal frictional force but a larger contact area on the inner artery surface. A larger contact area and radial force on the artery indicated enhanced attachment of the stent struts to the vessel walls, while a low longitudinal frictional force indicates proper stent apposition. These findings underscore the suitability of the superelastic Ti22112 alloy for self-expanding stents.

The mean and alternating values of the first principal strains under the cyclic loading were calculated and the stents implanted into the stenotic artery were found to have significantly higher maximum mean strain and alternate strain values compared with the straight artery. This difference resulted from the atherosclerotic plaque, which is consistent with recent works (Dordoni et al., 2014; Lei et al., 2019). It can be concluded that the mean and alternate strain are mainly determined by oversizing. Notably, Pelton addressed a relatively distinctive effect in NiTi that its fatigue limit would increase with increasing mean strain (Pelton et al., 2008), which is rare in other metallic materials. In contrast, a recent study concluded that the required strain amplitude to achieve a fatigue life of 400 million cycles decreased with increasing mean strain with a monotonous but non-linear tendency (Cao et al., 2020). Therefore, the effect of mean strain on NiTi and other superelastic materials, such as Ti22112, still remains to be determined.

From the aspect of superelasticity, this work showed the good functionality of the new Ni-free Ti22112 self-expanding stent but the results obtained highly depend on the chosen oversizing ratio and the plaque shape. Currently, the favourable compliance of Ti22112 stents is ensured due to its excellent fit in the sheath and robust contact with the stenotic artery. However, particular attention to the higher stiffness of Ti22112 is essential, especially when the stents are required to be inserted in a smaller diameter, or need to conform to a more complicated plaque shape. For example, a curved artery with thrombosis can substitute the straight one and varies in the arterial curvature values (Conway et al., 2012). On the other

hand, as NiTi exhibits higher superelastic recovery than Ti22112, the latter may pose a risk of plastic deformation in some extreme cases. Thus, the curvature region of a stent graft and the graft cross section can be adjusted to optimize stress concentration to avoid plastic deformation in future designs.

Conversely, a better understanding of the deformation mechanisms for new  $\beta$ -Ti alloys under various loading states will improve the accuracy of the FEA results, especially in scenarios involving complex structure and boundary conditions. Moreover, the fatigue performance of the stents was not considered in the present study. To evaluate the fatigue limit of the new materials, the in vitro tests on the specific devices manufactured in such materials should be considered to mimic the complicated loading procedure. The multi-axial fatigue criterion should also be carefully selected to measure the critical point and predict the fatigue life of the structure. Finally, the vascular model herein has an idealized geometry and only one sort of stent design was employed. A main concern during stent implantation emphasizes the flexibility of the stent. Indeed, lack of flexibility may cause a straightening effect on the vessel surface. One of the possible methods is to change the straight link into a “V”, “N” and “W” shape.

## **6. Conclusion**

Despite numerous experimental and clinical studies carried out on NiTi endovascular stents, the problem of nickel must be addressed for patients developing allergic reactions or hypersensitivity to this metal. Therefore, the development of new Ni-free cardiovascular stents is of crucial importance in the field of biomedical devices. In this study, the mechanical performance of self-expanding stents made with two new recently developed biocompatible titanium alloys (Ti-22Zr-11Nb-2Sn and Ti-24Zr-10Nb-2Sn alloy compositions) that exhibit superelastic properties was evaluated by finite element analysis and compared to NiTi. It should be noted that, to our knowledge, no finite element analysis study of these  $\beta$ -Ti medical devices is reported in the current literature. After selecting a self-expanding stent model, simulations by finite element analysis of the stents deployment and cyclic bending were implemented in a stenotic artery compared with a straight artery. Multiple numerical variables including stents strain distribution, artery diameter change, and total contact results were analysed to highlight differences between materials.

Our results show that after three cyclic bending, the Ti-22Zr-11Nb-2Sn self-expanding stent produced the largest contact area and radial contact force on the plaque and the highest increase in the stenotic artery diameter than the NiTi and Ti-24Zr-10Nb-2Sn stents. The

present work highlights that the new  $\beta$ -Ti alloys has enough crimping capacity and can better hold up the stenotic vessel compared with the NiTi stents. On the other hand, the stenosis plaque was found to play a significant role in the contact results and distribution of strain, which should not be neglected to avoid overestimation of the stent functionality. In addition, the total radial contact force between the stent and arterial system was found to correlate with the increment in the vessel diameter. Because only straight simplified artery and one plaque were concerned in this work, further extensions can be established to higher oversizing configurations, more loading conditions, longer service time, and more appropriate fatigue criteria.

To conclude, the Ti-22Zr-11Nb-2Sn stent demonstrated sufficient crimping capacity and reliable mechanical performance during deployment and cyclic bending, which could make it a suitable choice for self-expanding cardiovascular stents. In this work, the implementation of finite element analysis has thus made it possible to propose a solid basis for the mechanical evaluation of these stents fabricated with new Ni-free superelastic  $\beta$ -Ti alloys.

## Acknowledgement

T.Y. Jia acknowledges the China Scholarship Council of PRC for the Ph.D. financial support (Grant Number: 202108220010).

## References

- Amoroso, G., Van Geuns, R.-J., Spaulding, C., Manzo-Silberman, S., Hauptmann, K.E., Spaargaren, R., García-García, H.M., Serruys, P.W., Verheye, S., 2011. Assessment of the safety and performance of the STENTYS self-expanding coronary stent in acute myocardial infarction: results from the APPOSITION I study. *EuroIntervention* 7, 428–436. <https://doi.org/10.4244/EIJV7I4A71>
- Auricchio, F., Conti, M., De Beule, M., De Santis, G., Verheghe, B., 2011. Carotid artery stenting simulation: From patient-specific images to finite element analysis. *Med. Eng. Phys.* 33, 281–289. <https://doi.org/10.1016/j.medengphy.2010.10.011>
- Cabon, G., 2021. Caractérisations mécanique et microstructurale de nouveaux alliages de titane présentant une transformation martensitique pour la réalisation d'endoprothèses vasculaires. Ph.D Thesis, INSA Rennes.
- Cao, H., Wu, M.H., Zhou, F., McMeeking, R.M., Ritchie, R.O., 2020. The influence of mean strain on the high-cycle fatigue of Nitinol with application to medical devices. *J. Mech. Phys. Solids* 143, 104057. <https://doi.org/10.1016/j.jmps.2020.104057>
- Chen, C., Chen, J., Wu, W., Shi, Y., Jin, L., Petrini, L., Shen, L., Yuan, G., Ding, W., Ge, J., Edelman, E.R., Migliavacca, F., 2019. In vivo and in vitro evaluation of a

- biodegradable magnesium vascular stent designed by shape optimization strategy. *Biomaterials* 221, 119414. <https://doi.org/10.1016/j.biomaterials.2019.119414>
- Conway, C., Sharif, F., McGarry, J.P., McHugh, P.E., 2012. A Computational Test-Bed to Assess Coronary Stent Implantation Mechanics Using a Population-Specific Approach. *Cardiovasc. Eng. Technol.* 3, 374–387. <https://doi.org/10.1007/s13239-012-0104-8>
- Dordoni, E., Meoli, A., Wu, W., Dubini, G., Migliavacca, F., Pennati, G., Petrini, L., 2014. Fatigue behaviour of Nitinol peripheral stents: The role of plaque shape studied with computational structural analyses. *Med. Eng. Phys.* 36, 842–849. <https://doi.org/10.1016/j.medengphy.2014.03.006>
- Duerig, T.W., Pelton, A.R., Stockel, D., 1999. An Overview of Nitinol Medical Applications. *Mater. Sci. Eng. A* 273, 149-160. [https://doi.org/10.1016/s0921-5093\(99\)00294-4](https://doi.org/10.1016/s0921-5093(99)00294-4)
- Gao, J.J., Thibon, I., Castany, P., Gloriant, T., 2020. Effect of grain size on the recovery strain in a new Ti–20Zr–12Nb–2Sn superelastic alloy. *Mater. Sci. Eng. A* 793, 139878. <https://doi.org/10.1016/j.msea.2020.139878>
- Gao, J.J., Thibon, I., Laillé, D., Castany, P., Gloriant, T., 2019. Influence of texture and transformation strain on the superelastic performance of a new Ti–20Zr–3Mo–3Sn alloy. *Mater. Sci. Eng. A* 762, 138075. <https://doi.org/10.1016/j.msea.2019.138075>
- Gastaldi, D., Morlacchi, S., Nichetti, R., Capelli, C., Dubini, G., Petrini, L., Migliavacca, F., 2010. Modelling of the provisional side-branch stenting approach for the treatment of atherosclerotic coronary bifurcations: effects of stent positioning. *Biomech. Model. Mechanobiol.* 9, 551–561. <https://doi.org/10.1007/s10237-010-0196-8>
- Gotman, I., 1997. Characteristics of Metals Used in Implants. *J. Endourol.* 11, 383–389. <https://doi.org/10.1089/end.1997.11.383>
- Grassi, C.J., 1991. Inferior vena caval filters: analysis of five currently available devices. *Am. J. Roentgenol.* 156, 813–821. <https://doi.org/10.2214/ajr.156.4.2003449>
- Ijaz, M.F., Kim, H.Y., Hosoda, H., Miyazaki, S., 2014. Effect of Sn Addition on Stress Hysteresis and Superelastic Properties of a Ti–15Nb–3Mo alloy. *Scripta Mater.* 72, 29-32. <https://doi.org/10.1016/j.scriptamat.2013.10.007>
- Krone, L., Mentz, J., Bram, M., Buchkremer, H.P., Epple, M., 2005. The Potential of Powder Metallurgy for the Fabrication of Biomaterials on the Basis of Nickel - Titanium: A Case Study with a Staple Showing Shape Memory Behaviour. *Adv. Eng. Mater.* 7(7), 613-619. <https://doi.org/10.1002/adem.200500029>
- Lei, L., Qi, X., Li, S., Yang, Y., Hu, Y., Li, B., Zhao, S., Zhang, Y., 2019. Finite element analysis for fatigue behaviour of a self-expanding Nitinol peripheral stent under physiological biomechanical conditions. *Comput. Biol. Med.* 104, 205–214. <https://doi.org/10.1016/j.compbimed.2018.11.019>
- LePage, W.S., Shaw, J.A., Daly, S.H., 2021. Effects of texture on the functional and structural fatigue of a NiTi shape memory alloy. *Int. J. Solids Struct.*, Special Issue dedicated to papers from the International Union of Theoretical and Applied Mechanics 2019 Symposium on “Phase Transformations in Shape Memory Materials: Modeling and Applications” 221, 150–164. <https://doi.org/10.1016/j.ijsolstr.2020.09.022>
- Liu, Y., Xie, Z., Van Humbeeck, J., Delaey, L., 1998. Asymmetry of stress–strain curves under tension and compression for NiTi shape memory alloys. *Acta Mater.* 46, 4325–4338. [https://doi.org/10.1016/S1359-6454\(98\)00112-8](https://doi.org/10.1016/S1359-6454(98)00112-8)
- Lu, H., De Winter, R.J., Koch, K.T., 2018. The STENTYS self-apposing stent technology in coronary artery disease: literature review and future directions. *Expert Rev. Med. Devices* 15, 479–487. <https://doi.org/10.1080/17434440.2018.1491305>

- Mazurkiewicz, Ł.A., Bukala, J., Małachowski, J., Tomaszewski, M., Buszman, P.P., 2021. BVS stent optimisation based on a parametric model with a multistage validation process. *Mater. Des.* 198, 109363. <https://doi.org/10.1016/j.matdes.2020.109363>
- Meoli, A., Dordoni, E., Petrini, L., Migliavacca, F., Dubini, G., Pennati, G., 2013. Computational Modelling of In Vitro Set-Ups for Peripheral Self-Expanding Nitinol Stents: The Importance of Stent–Wall Interaction in the Assessment of the Fatigue Resistance. *Cardiovasc. Eng. Technol.* 4, 474–484. <https://doi.org/10.1007/s13239-013-0164-4>
- Miyazaki, S., Kim, H.Y., Hosoda, H., 2006. Development and characterization of Ni-free Ti-base shape memory and superelastic alloys. *Mater. Sci. Eng. A* 438–440, 18–24. <https://doi.org/10.1016/j.msea.2006.02.054>
- Nikanorov, A., Smouse, H.B., Osman, K., Bialas, M., Shrivastava, S., Schwartz, L.B., 2008. Fracture of self-expanding nitinol stents stressed in vitro under simulated intravascular conditions. *J. Vasc. Surg.* 48, 435–440. <https://doi.org/10.1016/j.jvs.2008.02.029>
- Orgéas, L., Favier, D., 1998. Stress-induced martensitic transformation of a NiTi alloy in isothermal shear, tension and compression. *Acta Mater.* 46, 5579–5591. [https://doi.org/10.1016/S1359-6454\(98\)00167-0](https://doi.org/10.1016/S1359-6454(98)00167-0)
- Otsuka, K., Ren, X., 2005. Physical metallurgy of Ti–Ni-based shape memory alloys. *Prog. Mater. Sci.* 50, 511–678. <https://doi.org/10.1016/j.pmatsci.2004.10.001>
- Pant, S., Bressloff, N.W., Limbert, G., 2012. Geometry parameterization and multidisciplinary constrained optimization of coronary stents. *Biomech. Model. Mechanobiol.* 11, 61–82. <https://doi.org/10.1007/s10237-011-0293-3>
- Pavón, L.L., Kim, H.Y., Hosoda, H., Miyazaki, S., 2015. Effect of Nb content and heat treatment temperature on superelastic properties of Ti–24Zr–(8–12)Nb–2Sn alloys. *Scr. Mater.* 95, 46–49. <https://doi.org/10.1016/j.scriptamat.2014.09.029>
- Pelton, A., Schroeder, V., Mitchell, M., Gong, X., Barney, M., Robertson, S., 2008. Fatigue and durability of Nitinol stents. *J. Mech. Behav. Biomed. Mater.* 1, 153–164. <https://doi.org/10.1016/j.jmbbm.2007.08.001>
- Ramezannejad, A., Xu, W., Xiao, W.L., Fox, K., Liang, D., Qian, M., 2019. New insights into nickel-free superelastic titanium alloys for biomedical applications. *Curr. Opin. Solid State Mater. Sci.* 23, 100783. <https://doi.org/10.1016/j.cossms.2019.100783>
- Russ, J.B., Li, R.L., Herschman, A.R., Waisman, H., Vedula, V., Kysar, J.W., Kalfa, D., 2021. Design optimization of a cardiovascular stent with application to a balloon expandable prosthetic heart valve. *Mater. Des.* 209, 109977. <https://doi.org/10.1016/j.matdes.2021.109977>
- Šittner, P., Sedlák, P., Seiner, H., Sedmák, P., Pilch, J., Delville, R., Heller, L., Kadeřávek, L., 2018. On the coupling between martensitic transformation and plasticity in NiTi: Experiments and continuum based modelling. *Prog. Mater. Sci.* 98, 249–298. <https://doi.org/10.1016/j.pmatsci.2018.07.003>
- Steinemann, S.G., 1998. Titanium — the material of choice? *Periodontol.* 2000 17, 7–21. <https://doi.org/10.1111/j.1600-0757.1998.tb00119.x>
- Steinemann, S.G., 1996. Metal implants and surface reactions. *Injury* 27, S/C16-S/C22. [https://doi.org/10.1016/0020-1383\(96\)89027-9](https://doi.org/10.1016/0020-1383(96)89027-9)
- Stoeckel, D., Pelton, A., Duerig, T., 2004. Self-Expanding Nitinol Stents: Material and Design Considerations. *Eur. Radiol.* 14(2), 292–301. <https://doi.org/10.1007/s00330-003-2022-5>
- Vad, S., Eskinazi, A., Corbett, T., McGloughlin, T., Vande Geest, J.P., 2010. Determination of Coefficient of Friction for Self-Expanding Stent-Grafts. *J. Biomech. Eng.* 132, 121007. <https://doi.org/10.1115/1.4002798>

- Wever, D.J., Veldhuizen, A.G., Sanders, M.M., Schakenraad, J.M., Horn, J.R. van, 1997. Cytotoxic, allergic and genotoxic activity of a nickel-titanium alloy. *Biomaterials* 18, 1115–1120. [https://doi.org/10.1016/S0142-9612\(97\)00041-0](https://doi.org/10.1016/S0142-9612(97)00041-0)
- Wu, W., Qi, M., Liu, X.-P., Yang, D.-Z., Wang, W.-Q., 2007. Delivery and release of nitinol stent in carotid artery and their interactions: A finite element analysis. *J. Biomech.* 40, 3034–3040. <https://doi.org/10.1016/j.jbiomech.2007.02.024>
- Xu, J., Yang, J., Huang, N., Uhl, C., Zhou, Y., Liu, Y., 2016. Mechanical response of cardiovascular stents under vascular dynamic bending. *Biomed. Eng. OnLine* 15, 21. <https://doi.org/10.1186/s12938-016-0135-8>